Stability and Lattice Dynamics of Ruddlesden–Popper Tetragonal Sr 2 TiO 4

Romain Viennois, P. Hermet, D. Machon, M. Koza, D. Bourgogne, B. Fraisse, A. Petrović, D. Maurin

Stability and lattice dynamics of Ruddlesden-Popper tetragonal Sr_2TiO_4

R. Viennois[a,b,*], P. Hermet[a], D. Machon[c], M. M. Koza[d], D. Bourgogne[a], B. Fraisse[a], A. P. Petrović[b,1], D. Maurin[e]

[a] ICGM, Université Montpellier, CNRS, ENSCM, Montpellier, France

[b] Dep. Quantum Matter Phys., Univ. Geneva, Ecole de Physique, 24 quai Ernest Ansermet, CH-1211 Geneva, Switzerland

[c] Univ Lyon, Université Claude Bernard Lyon 1, CNRS UMR 5306, Institut Lumière Matière, F-69622 Villeurbanne, France

[d] Institut Laue Langevin, 71 Avenue des Martyrs, CS 20156, F-38042 Grenoble, France

[e] L2C, Université Montpellier, CNRS, Montpellier, France

Abstract

We report a combined experimental and theoretical lattice dynamics study of the Ruddlesden-Popper layered compound Sr_2TiO_4. From inelastic neutron scattering experiments we derive the generalized phonon density of states of Sr_2TiO_4. We also report its heat capacity, thermal expansion and the thermodynamic Grüneisen parameter using the calculated bulk modulus and find a large value of about 2. Using Raman scattering experiments under pressure, we discuss a probable structural distortion of the tetragonal structure above 11 GPa which could be due to non-hydrostatic compression. The mode Grüneisen parameters of the four Raman-active modes are determined and shown to be in reasonable agreement with those obtained by DFPT calculations. The temperature behavior of the Raman-active modes was studied, allowing us to determine the implicit volume and explicit anharmonic contributions. Above 400 K, the implicit volume contribution dominates the temperature-induced variation of the four Raman-active modes, whereas below this temperature, the explicit anharmonic contribution is the dominant contributor to the highest energy mode. Our results underline the importance of the anharmonicity in vibrational-related properties of Sr_2TiO_4.

* Corresponding author : romain.viennois@umontpellier.fr

[1] Current address: Division of Physics and Applied Physics, School of Physical and Mathematical Sciences, Nanyang Technological University, 21 Nanyang Link, 637371 Singapore.

I. Introduction

The Ruddlesden-Popper (RP) structure forms a family of layered body-centered tetragonal crystals (space group I4/mmm) with general formula $A_{n+1}M_nO_{3n+1}$, where A is an alkaline or rare-earth metal and M is a transition metal. [1,2] These structures are derived from cubic perovskites and can be viewed as a natural superlattice made by successively stacking *n* AMO_3 perovskite-type layers separated by one AO Rocksalt-type layer.

Ruddlesden-Popper compounds with *n* = 1 display a wide variety of microscopic transport properties, making them very interesting for technological applications in the energy and photonics sectors. In particular, we highlight high-temperature superconductivity[3,4]; thermoelectricity, photoconductivity and photocatalysis in titanates[5-12]; protonic and/or oxygen conduction in titanates[13,14] and nickelates[15,16] ; and a range of optical properties, especially photoluminescence in titanates.[17-19] During the last decade, various complex correlated properties have been discovered in Sr_2MO_4 compounds with d-electrons around the Fermi level. [20-35] Several of these compounds are Mott insulators. [20-24] More interestingly unconventional superconductivity with broken time-reversal symmetry was discovered in Sr_2RuO_4 [28-30]and complex 2D spin-orbital ordering was found in Sr_2IrO_4[24,25] and Sr_2VO_4. [31-35] In this latter case, the exact nature of this coupling remains to be understood. [31-35]

Despite these interesting electronic properties, the vibrational properties of these compounds have been poorly investigated and are far from being understood despite their importance in the understanding of the properties of these A_2MO_4 compounds. The aim of the present work is to combine both theoretical and experimental approaches to study the lattice dynamics of the simplest of these compounds, Sr_2TiO_4, in which the titanium d-orbitals are empty.

In the past, relatively few works investigating the lattice dynamics of Sr_2TiO_4 and its related properties have been performed. These mainly focused on the study of phonons at the Brillouin zone center by means of infrared-spectroscopy [36-38]and Raman spectroscopy. [36,37,39-41] The phonon dispersion curves and density of phonon states have only been recently reported using DFT calculations. [42-44] Several additional DFT works investigated the elastic constants of Sr_2TiO_4 using stress-strain methods, although discrepancies of ~10 % were found between those studies. [45-47]

However, these investigations were incomplete: in the case of infrared experiments, the low temperature regime was only briefly investigated using thin films[38], and in the case of Raman spectroscopy experiments, the pressure dependence was only explored in a limited range up to 7 GPa. [41] Beyond infrared and Raman techniques, preliminary inelastic neutron scattering experiments have also been reported. [48] Finally, the high-temperature thermal expansion (a vibrational-related property) of Sr_2TiO_4 was recently studied by neutron powder diffraction (NPD) and Synchrotron X-ray diffraction (XRD) experiments[49] as well as DFT calculations. [43,47]

In this work, we report an extensive study of the lattice dynamics in Sr_2TiO_4 as a function of pressure and temperature. We first discuss the harmonic lattice dynamic properties from density functional perturbation theory (DFPT) calculations and inelastic neutron scattering, Raman spectroscopy and heat capacity experiments. Then, we present the elastic constants derived with DFPT. Finally, we study the anharmonicity of the lattice dynamics of Sr_2TiO_4 by means of thermal expansion and a complete set of Raman spectroscopy data over a wide range of temperatures and pressures. Our results highlight the importance of the anharmonicity in vibrational related properties of Sr_2TiO_4.

II. Experimental details

Ceramic samples of Sr_2TiO_4 were obtained from a stoichiometric mixture of 99.999 % $SrCO_3$ and 99.99 % TiO_2. The mixture was initially ball-milled and mixed for several hours in an agate jar, then calcined at 1200°C for 12 h. In a second step, the obtained product was again ball-milled and mixed over several hours, before sintering for 12 h at 1100°C. The resulting product was a single-phase Sr_2TiO_4 specimen, as shown by X-ray diffraction (XRD) characterization (see Fig. 1). The room temperature XRD experiment was performed with a PW1820 Philips diffractometer using copper $K_{\alpha1}$ and $K_{\alpha2}$ wavelengths and a 0.02° step. The lattice parameter and atomic positions were derived from a Rietveld refinement of the XRD patterns using the Fullprof software. [50] We derive the lattice parameters a = 3.88267(2) Å ; c = 12.5838(1) Å, in good agreement with published results (a = 3.88656 Å ; c = 12.5975 Å [49] or a = 3.8812 Å ; c = 12.601 Å [51]).

High temperature XRD experiments were performed with a Seifert diffractometer using copper $K_{\alpha 1}$ and $K_{\alpha 2}$ wavelengths and a 0.04° step. The heating was accomplished using a Pt plate as heater and the temperature was measured with a $Pt/Rh_{0.1}Pt_{0.9}$ S type thermocouple.

Raman scattering experiments under high pressure were performed using a homemade Raman spectrometer equipped with a Peltier cooled CCD and a green laser (λ = 514.5 nm). High pressure measurements were performed within a membrane diamond anvil cell (DAC) with low fluorescence diamonds. The samples were placed into a 125 µm chamber drilled in an indented stainless-steel gasket. The transmitting medium was a methanol:ethanol mixture with a 1:4 ratio, maintaining hydrostatic conditions up to 10 GPa. The fluorescence of ruby was used as a pressure gauge. [52]

Raman scattering experiments below room temperature were performed in a Horiba Jobin-Yvon T64000 spectrometer equipped with a liquid N_2 cooled CCD and an Ar^+ laser (λ = 514.5 nm). The low temperature measurements were performed in an Oxford Helium microstat under the objective lens (X50) of an Olympus microscope. The temperature was measured with a Si diode.

Raman scattering experiments above room temperature were performed in a Horiba Jobin-Yvon Labram Aramis spectrometer equipped with a Peltier cooled CCD and a blue diode laser (λ = 473 nm). High temperatures were attained using the oven of a Linkham TS1500 heating stage under the objective lens (X50) of an Olympus microscope. The temperature was measured with a Pt resistance thermometer at the bottom of the oven.

In all the Raman experiments, the spectra were obtained in a backscattering configuration using a microprobe device which allowed the incident light to be focused into a spot of diameter several microns on the sample.

The inelastic neutron scattering (INS) experiments were performed at room temperature with a powder sample using the high-resolution IN6 time-of-flight (TOF) spectrometer at the Institute Laue Langevin in Grenoble, France. An incident neutron wavelength of 4.14 Å was utilized, offering an elastic resolution of about 0.2 meV. Standard corrections for background, sample holder, detector efficiency and self-attenuation have been applied to the TOF signal. The corrected response has been transformed to the dynamic structure factor by established computational routines within the software package

LAMP. The generalized density of states (GDOS) has been computed from the dynamic structure factor within the incoherent approximation.[53]

Heat capacity experiments were performed in a Physical Property Measurement System (PPMS) cryostat from Quantum Design, using a short relaxation method.

III. Computational details

The first-principles calculations were performed by means of density functional theory (DFT) and the local density approximation (LDA) using the ABINIT package. [54] We used highly transferable norm-conserving Teter pseudopotentials. [55] Strontium 4s, 4p and 5s electrons, Ti 3s, 3p, 3d and 4s electrons and O 2s and 2p electrons were treated as valence states.

The plane wave energy cutoff was 60 Ha. Brillouin zone integration was performed using a 8x8x8 Monkhorst-Pack mesh for the calculation of the zone-center phonon modes, while a 12x12x12 mesh was used to compute the formation energy and the electronic band gap. The structural relaxation was performed in the primitive body-centered tetragonal unit cell, until the maximum residual forces on each atom were less than $6x10^{-6}$ Ha/Bohr and the pressure was less than $2x10^{-8}$ Ha/Bohr^3. From our DFT calculations with the LDA exchange-correlation functional, we find lattice parameters a = 3.8217 Å and c = 12.3145 Å, which are about 2 % lower than our experimental results and prior results in the literature [49,51]. In contrast, our c/a ratios are almost the same (c/a = 3.2223 in DFT against c/a = 3.241 in our experiments and 3.241 [49], 3.247 [51] in prior experiments). Our results agree well with prior LDA calculations performed by Fennie and Rabe. [42] The dynamical matrix, dielectric constants, Born effective charges and elastic constants have been calculated using a variational approach to density functional perturbation theory. [56] Phonon dispersion curves are interpolated according to the scheme described by Gonze et al. [57] In this method, the dipole-dipole interactions are subtracted from the dynamical matrix before the Fourier transformation, so that only the short-range part is handled in the real space. A 4x4x4 q-grid in the irreducible Brillouin zone is employed for the calculations of the vibrational dispersion curves, while a denser 90x90x60 q-grid is used for the calculation of the phonon density of states and the thermodynamic functions. The Raman susceptibility tensors are obtained within

a non-linear formalism using the 2n+1 theorem. [58] The infrared transmittance, infrared reflectivity and Raman spectra are calculated as described in refs. [59-61]. The isothermal mode Grüneisen parameters at the Brillouin zone center have been calculated via a finite differences method using $\gamma_i^T = \frac{B}{\omega_i}\frac{\Delta\omega_i}{\Delta P}$, by computing the frequencies at two additional different pressure P = -1 GPa and 1 GPa, reoptimizing the lattice parameters and the atomic positions, then using the bulk modulus B obtained by DFPT calculations.

IV. Results and discussion

1) Lattice dynamics

a) Acoustic phonons

We report in Table 1 the DFT results of the elastic constants C_{ij}. From these C_{ij}, we have calculated the bulk modulus B_h, the shear modulus G_h, the Young's modulus E_h and Poisson's coefficient ν_h within the Hill approximation. [62] Our results differ from two recent works where a Perdew-Burke-Ernzerhof (PBE) exchange-correlation functional was used. [45,46] This is certainly related to the use of different exchange-correlation functionals. Indeed, using the LDA exchange-correlation functional, we find larger elastic constants due to the smaller lattice parameters in our calculations. We expect that the experimental value will lie between our results and those obtained with a PBE exchange-correlations functional. We find a ratio $B_h/G_h = 1.778$, which is larger than the value of 1.75 proposed for the boundary between brittle and ductile materials. [63] This means that Sr_2TiO_4 is slightly ductile and lies close to this boundary. This is surprising because ductile materials are generally metallic, whereas brittle materials are semiconducting. [63,64]We find a powder-averaged Poisson's coefficient $\nu_h = 0.263$, a value similar to those found in ZnSb or GaSb and typical of materials whose bonding is more covalent than ionic. [64] The knowledge of the Cauchy pressures also gives an insight into the bonding character along the different crystal directions of a material. [64] The Cauchy pressures in the *ab* plane and along the *c* axis can be defined as $P_{xy} = C_{23} - C_{44}$ and $P_z = C_{12} - C_{66}$, respectively. In the case of Sr_2TiO_4, one finds $P_{xy} = 18.3$ GPa and $P_z = -14.5$ GPa. Thus, the rather large and positive value of the Cauchy pressure in the *ab* plane is more characteristic of ionic compounds, whereas the rather large and negative value of the Cauchy pressure

in the *c* direction is characteristic of covalent materials. [64] This means that the bonds are more directional and have a more covalent character in the *c* direction than in the *ab* plane. Despite this bonding anisotropy, one can determine [65] that the anisotropy of the bulk modulus $\frac{B_a}{B_c} = \frac{(C_{11}-C_{33})+(C_{12}-C_{13})}{(C_{33}-C_{13})}$ is as low as 1.021, and therefore that Sr_2TiO_4 has a quasi-isotropic bulk modulus.

b) Optical phonons at the Brillouin zone center

There are 7 atoms in the primitive unit cell and therefore 21 phonon modes, including 3 acoustic and 18 optical phonon modes. The decomposition into irreducible representations of the optical modes is: $\Gamma = 2\ A_{1g} \oplus 2\ E_g \oplus 3\ A_{2u} \oplus 4\ E_u \oplus B_{2u}$. We report in Table 2 our results for the phonon energies at the Γ point. There are 4 Raman-active modes with A_{1g} and E_g symmetries, and 7 infrared-active modes with A_{2u} and E_u symmetries. Our calculations are in very good agreement with those of Fennie and Rabe for the fully-relaxed cell, also based on the LDA exchange correlation. [42]

We report in Figure 2 the experimental Raman spectrum of Sr_2TiO_4 at 20 K, together with the DFPT-calculated spectrum. There is a good agreement between experiments and calculations for both the positions and the relative intensities of the Raman lines located at 125 cm^{-1}, 210 cm^{-1}, 280 cm^{-1} and 570 cm^{-1}. Table 2 shows the exact frequencies of the Raman modes in both experiments and calculations. The broader lines observed at 400-450 cm^{-1} and 700 cm^{-1} have been previously reported and are probably due to some second order Raman modes or defect-induced excitations. [36,37,40,41] In the latter case, given the high frequencies of the modes and the broadness of these peaks, they are more likely to originate from defects on the O sub-lattice. Concerning the infrared-active modes, there is a reasonable agreement between calculations and experiments [37,40] for the four bands below 300 cm^{-1}, but a rather poor agreement concerning the three modes above 300 cm^{-1}. However, for these high-frequency modes, even the two experimental reports yield inconsistent frequencies. [37,40]

c) Lattice dynamics in the full Brillouin zone

In Figure 3, we report the phonon dispersion curves, as well as the total and atom-projected phonon densities of states (DOS) of Sr_2TiO_4. The shoulder at 95 cm^{-1} is due to the flattening of the transverse

acoustic modes at the Brillouin zone boundaries. The peak at 120 cm^{-1} is due to the flattening of the longitudinal acoustic mode at the Brillouin zone boundaries as well as the lower energy optical mode with E_g symmetry at the Γ point, which is a Raman-active vibration in the *ab* plane. The next two peaks in the phonon DOS at 160 and 175 cm^{-1} are due to the next-lowest energy optical mode with E_u symmetry, which is an infrared-active vibration in the *ab* plane. The subsequent features in the phonon DOS up to 575 cm^{-1} are due to many different optical branches. The last two features in the phonon DOS originate from the higher energy optical mode which is an infrared-active vibration in the *ab* plane, with the peak at about 850 cm^{-1} caused by the dispersion of the LO mode. The phonon DOS is dominated below 140 cm^{-1} by Sr vibrations, between 140 and 210 cm^{-1} by Sr and O, between 210 and 570 cm^{-1} by O and Ti, and almost exclusively by O above 570 cm^{-1}.

When comparing our results with those of Huang et al, [43] we find significant differences, especially at low frequencies. Notably, they found an optical mode at about 2 THz, i. e. about 67 cm^{-1}, in contrast with our calculations and Fennie's work [42] in which the lowest energy optical mode is at about 124 cm^{-1}.

For comparing our calculations with the experimental Generalized Density of States (GDOS) obtained from Inelastic Neutron Scattering (INS) experiments, we calculate the weighted neutron density of states $Z'(E)$ using : $Z'(E) = \sum_i \frac{\sigma_i}{M_i} Z_i(E)$, where $Z_i(E)$ are the atom-projected density of states, σ_i are the scattering cross sections and M_i are the atomic masses of each atom.

The GDOS and Z'(E) are shown in Figure 4. There is a qualitative agreement up to 550 cm^{-1} and especially below 300 cm^{-1}, with a good correspondence between the positions of the different peaks and shoulders in the spectral densities. However, above 550 cm^{-1}, the agreement is quite poor. This may be due to the presence of O sublattice defects in the samples, as suggested by the additional broad bands in the Raman spectra, which are likely associated with the presence of defects.

d) Heat capacity

The heat capacity of Sr_2TiO_4 is reported in Figure 5, where our experimental results below 300 K together with Jacobs' results above 300 K [66] are compared with our DFPT calculations. The agreement

is rather good up to 650 K. Above this temperature the experimental heat capacity is larger than the calculated one and increases linearly with temperature, whereas the calculated heat capacity saturates to the Dulong-Petit limit of 174.6 J/mole.K. Indeed, in the DFPT calculations, we calculate the heat capacity C_v at constant volume, whereas the experimental data correspond to the heat capacity C_P at constant pressure. The difference between the two terms $C_P - C_V$ is equal to $\alpha_V^2 BVT$. Unfortunately, although the thermal expansion has been measured (see ref. 70 and below), this is not the case for the bulk modulus. With B obtained by DFPT calculations, we compute $C_P - C_V$ = 26.9 J/mole.K at 1600 K. This is the same order of magnitude as the difference between the experimental and calculated data (12.94 J/mole.K).

2) Raman scattering under pressure

The Raman spectra of Sr_2TiO_4 as a function of pressure are shown in Figure 6. In contrast to the study reported in ref. [41], which was limited to 7 GPa, we can observe Raman spectra with good signal-to-noise ratio up to the maximum pressure of 31 GPa. There is a broadening of the Raman peaks with increasing pressure. Above roughly 11-13 GPa, we observe the appearance of a new peak at about 200 cm^{-1}, a shoulder at about 660 cm^{-1}, and the decay of the small peak from the lowest energy Raman mode E_g at about 127 cm^{-1}. Above 14.5 GPa, a third new weak peak appears at 157 cm^{-1}. We also note that the broad peak at 520-570 cm^{-1} increases in intensity at high pressure. One cannot exclude that this peak is due to a new, first-order Raman mode. These new peaks could be related to a structural distortion of the tetragonal structure above 11 GPa. In a recent theoretical study, a phase transition was found upon compression from the I4/mmm structure stable at ambient conditions to the Cmcm structure, although at much higher pressure (66.6 GPa). [67] However, the observed modification shows little change in the Raman spectra and may instead be related to a distortion associated with non-hydrostatic compression. The pressure variation of the different mode frequencies is linear at low pressures and can be described by a 2nd order polynomial function, similarly to the case of silicon. [68] The pressure derivatives $d\omega/dP$ of the four Raman-active modes derived from polynomial fits are reported in Table 4. These values and their trend compare well with data obtained by Venkastewan, [41] except for the highest energy A_{1g} mode,

for which we find a 20 % larger value. From the knowledge of dω/dP, it is possible to determine the mode Grüneisen parameter. This will be discussed below.

3) Temperature dependent properties

a) Raman scattering

We report in Figure 7 several selected Raman spectra between ambient temperature and 1473 K. The thermal variation of the frequencies and the full-width at half-maximum (FWHM) of the four Raman-active modes are reported in Figures 8 and 9. For the three lowest energy modes, a monotonic decrease of the peak positions with increasing temperature is visible. The behavior of the highest energy mode is more complex, with an upshift of the peak position from the lowest temperature up to about 200 K where it reaches a maximum, followed by a downshift above 200 K. We will quantitatively discuss the different contributions below.

b) Thermal expansion and the thermodynamic Grüneisen parameter

The thermal variation of the lattice parameters *a* and *c* of Sr_2TiO_4 is shown in Figure 10. The error bars of the lattice parameters are within the symbol size. From calibration measurements, the error of the temperature measurements has been estimated to be about 20 K at 900 K. One can see that at higher temperatures (from 1000 to 1400 K), the increase of the lattice parameters with temperature is stronger than linear. The ratio *c*/*a* is 3.239 at room temperature and increases slightly to 3.241 between 1000 K and 1200 K, but stays constant above 1200 K. Kawamura et al have determined the thermal expansion coefficients ($\alpha_x = (da/dT)/a$, $\alpha_z = (dc/dT)/c$ and $\alpha_V = 2\,\alpha_x + \alpha_z$) from the change of the lattice parameters between 300 K and 1300 K and found $\alpha_x = 12.25\ MK^{-1}$, $\alpha_z = 12.7\ MK^{-1}$ and $\alpha_V = 37.2\ MK^{-1}$. [49] Applying the same procedure we find slightly lower values: $\alpha_x = 12.09\ MK^{-1}$, $\alpha_z = 12.34\ MK^{-1}$ and $\alpha_V = 36.52\ MK^{-1}$. These reinforce Kawamura *et al.*'s finding that the thermal expansion is weakly anisotropic in Sr_2TiO_4 with $\alpha_x < \alpha_z$. Parameters derived from polynomial fits to the thermal variation of the thermal expansion coefficients α_x, α_z and α_V are reported in Figure 11. An estimation of the error bar is given at 900 K. One can see that the thermal expansion coefficients increase with temperature and are rather

large. Between room temperature and 1700 K, α_z increases by about 45 %, which is much higher than the approximate 25 % increase in α_x. Over the same temperature range, α_V increases from 32.2 MK^{-1} to 42.2 MK^{-1}, which is higher than in $SrTiO_3$ where an average of 32.2 MK^{-1} is reported between 300 and 2000 K. [69]

To shed light on the anharmonicity of Sr_2TiO_4, we compute the thermodynamic Grüneisen parameter $\Gamma = \alpha_V B/VC_P$ [70] from the experimentally-determined parameters α_V, molar volume V, and heat capacity C_P as well as the DFPT-calculated bulk modulus B (see Table 1). The results are reported in the inset of Figure 12. At room temperature, Γ is about 2. Note that using the bulk modulus B of Music *et al*, [60] one derives a value of 1.75. Γ is increasing slightly at the highest temperature. The thermodynamic Grüneisen parameter Γ is rather large, meaning that the anharmonicity is significant in Sr_2TiO_4. We have also determined the thermodynamic Grüneisen parameters in the *x* and *z* directions, Γ_x and Γ_z as follows: [70,71]

$$\Gamma_x = \frac{V}{C_P}[(C_{11} + C_{12}).\alpha_x + C_{13}.\alpha_z] \text{ and } \Gamma_z = \frac{V}{C_P}[2C_{13}.\alpha_x + C_{33}.\alpha_z] \qquad (12)$$

using elastic constants C_{ij} calculated by DFPT. As can be seen in the inset of Figure 12, the anisotropy of the Grüneisen parameters is weak in Sr_2TiO_4, meaning that the anharmonicity is similar in both the *ab* plane and the *c* direction.

4) Mode Grüneisen parameters and anharmonicity

In the harmonic approximation, the frequencies of the vibrational modes are constants and do not change with volume, pressure or temperature. In the quasi-harmonic approximation, the frequencies of the vibrational modes vary upon volume change and therefore also upon temperature and pressure variations.

The thermal variation of the mode frequencies ω_i is divided into two contributions, yielding: [72,73]

$$\omega_i(T) = \omega_i(T = 0\ K) + \Delta\omega_i^{impl} + \Delta\omega_i^{expl} \qquad (1)$$

Here $\Delta\omega_i^{impl}$ is the implicit contribution accounting for the volume dependence of the mode frequencies, and $\Delta\omega_i^{expl}$ is the explicit contribution determined by the thermal population of the vibrational levels which depends on the anharmonicity.

In the isotropic Grüneisen approximation, one can define the isothermal Grüneisen parameter γ_i^T and the isobaric Grüneisen parameter γ_i^P of the i[th] mode as: [72,73]

$$\gamma_i^T = B\left(\frac{\partial ln\omega_i}{\partial P}\right)_T \text{ and } \gamma_i^P = \frac{-1}{\alpha_V}\left(\frac{\partial ln\omega_i}{\partial T}\right)_P \qquad (2)$$

The isobaric Grüneisen parameter can be expressed as: [73]

$$\gamma_i^P = \gamma_i^T + \gamma_i^V \qquad (3)$$

One can apply the isotropic approximation because the bulk modulus is almost isotropic, as is the thermal expansion. Using Raman scattering experiments under high pressure, one can determine the isothermal Grüneisen parameters γ_i^T; while using Raman experiments as a function of temperature, one can determine the isobaric Grüneisen parameters γ_i^P. When the quasi-harmonic approximation can be strictly applied, $\gamma_i^V = 0$ and $\gamma_i^P = \gamma_i^T$. Therefore, in the general case, γ_i^V is a measure of the anharmonic contribution to the frequency shift, i.e. the explicit effect, whereas γ_i^T corresponds to the volume contribution, i.e. the implicit effect. One can thus define the implicit fraction $\eta_i = \gamma_i^T/\gamma_i^P$ and evaluate the magnitude of the implicit and explicit contributions to each mode.

Using the bulk modulus computed by DFPT, one can determine the isothermal Grüneisen parameters γ_i^T of the different Raman-active modes, which are given in Table 3. We have also performed DFPT calculations of the isothermal Grüneisen parameters γ_i^T of the different modes at the Brillouin zone center. The theoretical results are given in Table 4. In the case of the Raman-active modes (see Table 3), there are some significant disagreements for the lowest energy E_g and A_{1g} modes (about 15-20 %), but a good agreement for the highest energy E_g and A_{1g} modes (about 3-5 %). Moreover, the theoretical calculations provide a good reproduction of the experimental trend. The values of the two lowest Raman-active energy modes (involving mainly Sr motions) are larger than the value of the thermodynamic Grüneisen parameter Γ, and about two times larger than those of the two highest energy Raman-active modes (for which the contribution of the oxygen atoms in the SrO layers is predominant). This means that the two lowest energy Raman-active modes are more anharmonic than the two highest energy Raman-active modes, and thus that vibration modes involving Sr atoms are the most anharmonic ones, contributing much more strongly to the thermal expansion. In contrast, the optically silent mode B_{2u}

(which involves only *c*-axis motion of the oxygen atoms in the TiO_2 layer) has a very low Grüneisen parameter, and therefore very weak anharmonicity.

In Fig. 8, for the three lowest energy Raman-active modes one observes a monotonic decrease of the peak positions with increasing temperature. We note that the Raman shift of the highest E_g mode stays constant from the lowest temperature up to 300 K, which indicates that the explicit and implicit contributions have opposite signs, cancelling out each other in this temperature range. The peak position of the highest energy A_{1g} mode upshifts from the lowest temperature up to about 200 K where it reaches a maximum, followed by a downshift above 200 K. The behavior of this mode can be explained by the opposite signs of the implicit and explicit contributions. As the isothermal Grüneisen parameter γ_i^T of the highest energy mode is positive, the implicit volume term $\Delta\omega_i^{\text{impl}}$ is negative, which means that the explicit anharmonic term $\Delta\omega_i^{\text{expl}}$ should be positive and even the largest contribution, at least up to 200 K.

Since the thermal variation of the different modes is linear from room temperature until at least 800 K, one can determine the isobaric Grüneisen parameter γ_i^P from the slope obtained by a linear fit of the thermal variation of the frequencies (with the knowledge of the thermal expansion). Now, knowing both γ_i^P and γ_i^T, one can deduce γ_i^V and η_i of each Raman-active mode. The results are given in Table 3. All modes γ_i^V have negative values, meaning that the explicit anharmonic terms $\Delta\omega_i^{\text{expl}}$ have positive values for the 300-800 K temperature range. In this temperature range, the ratio η_i is much larger than 0.5, which means that the implicit volume contribution is the dominant contribution in the temperature dependence of the frequencies of the Raman-active modes of Sr_2TiO_4. The large values of the ratio η_i of the Raman-active modes found in Sr_2TiO_4 are typical of ionic materials, e. g. alkaline-earth fluorides [74-76], a conclusion different from that which we obtain from the Poisson coefficient. However, as discussed above, the explicit anharmonic contribution is dominant at least up to 200 K for the highest energy mode. This is due to the low Grüneisen parameter of this mode. Both the large explicit contribution and the low mode Grüneisen parameter of this A_{1g} mode (involving *c*-axis O motion) indicate that bonding in this direction is less ionic/more covalent. This observation is in good agreement

with our previous analysis of the Cauchy pressure, indicating less ionic/more covalent bonding in the *c* direction.

In order to better account for the thermal variation of the implicit and explicit contributions, we assume that the Grüneisen parameters are independent of the temperature and correspond to the isothermal Grüneisen parameters γ_i^T. One can then determine both contributions (in the isotropic approximation) as follows: [72,73,77]

$$\omega_i^{impl} = \omega_i(T = 0K).\, e^{-\gamma_i^T \int_0^T \alpha_V(T)dT} \qquad (4)$$

If we assume that the volume thermal expansion α_V is independent of the temperature, we obtain:

$$\omega_i^{impl} = \omega_i(T = 0K).\, e^{-\gamma_i^T \alpha_V T} \qquad (5)$$

$$\omega_i^{expl} = A\left(1 + \frac{2}{e^x - 1}\right) + B\left[1 + \frac{3}{e^y - 1} + \frac{3}{(e^y - 1)^2}\right] \qquad (6)$$

where $x = \frac{\hbar\omega}{2k_BT}$ and $y = \frac{\hbar\omega}{3k_BT}$.

Using the constant value of the volume thermal expansion determined between 300 K and 1273 K, α_V = 36.52 MK^{-1}, one can determine the implicit quasi-harmonic contribution from eq. (5) and hence deduce the explicit anharmonic contribution. The results are given in Figure 12, together with the fitting of the explicit contribution with eq. (6). We note that for all the modes, A > 0 and B < 0.

The FWHM Δ_i of the Raman modes can be expressed as a function of the residual term $\Delta(0)$, the 3-phonon interaction term Δ_3 and the 4-phonon interaction term Δ_4: [72,73,77]

$$\Delta_i = \Delta(T = 0\ K) + \Delta_3 + \Delta_4 \qquad (7)$$

where the term $\Delta(T = 0\ K)$ is constant, and [88,89,93]

$$\Delta_3 = C\left(1 + \frac{2}{e^x - 1}\right) \text{ and } \Delta_4 = D\left[1 + \frac{3}{e^y - 1} + \frac{3}{(e^y - 1)^2}\right] \qquad (8)$$

We show the results of modeling the FWHM Δ_i using eqs. (7-8) in Figure 9. It is difficult to draw quantitative conclusions for the lowest Raman-active mode since the FWHM have large errors, especially at high temperature. However, our data indicate that C and D are positive for the three lowest energy modes, whereas $C > 0$ and $D < 0$ for the highest energy mode.

Conclusion

We have reported a combined experimental and theoretical study of the lattice dynamics in the Ruddlesden-Popper layered compound Sr_2TiO_4. We have measured the generalized phonon density of states of Sr_2TiO_4 using inelastic neutron scattering experiments as well as the pressure and temperature dependence of the Raman-active modes of Sr_2TiO_4. We have determined a rather large thermodynamic Grüneisen parameter of about 2 from the heat capacity and thermal expansion experiments, using the calculated bulk modulus. From our Raman scattering experiments under pressure, we report a probable structural distortion of the tetragonal structure above 11 GPa which could be due to non-hydrostatic compression. There is a reasonable agreement between the experimental mode Grüneisen parameters of the Raman-active modes with those obtained by DFPT calculations. The mode Grüneisen parameters of the two lowest energy Raman-active modes involving mainly Sr atoms are two times larger than the two highest energy Raman-active modes. By determining the pressure and temperature dependence of the Raman-active modes, we were able to determine their implicit volume contributions and explicit anharmonic contributions. Above 400 K, the implicit volume contribution dominates the temperature behavior of all four Raman-active modes. This is typical of ionic materials, but contradicts the conclusion drawn from the Poisson coefficient. However, our analysis of the Cauchy pressures indicates that the bondings are more ionic in the ab plane than in the c direction. Therefore, one can consider Sr_2TiO_4 to exhibit iono-covalent bondings. Below 400 K, the explicit anharmonic contribution is dominant for the highest energy mode, which mainly involves motion of the oxygen atoms along the *c* direction. This means that these bondings are less ionic/more covalent, in agreement with our analysis of the Cauchy pressures.

References

[1] Ruddlesden, S. N. ; Popper, P. New compounds of the K_2NiF_4 type. *Acta Cryst.* **1957**, *11*, 538-539.

[2] Ruddlesden, S. N. ; Popper, P. The compound $Sr_3Ti_2O_7$ and its structure. *Acta Cryst.* **1958**, *11*, 54-55.

[3] Bednorz, J. G. ; Müller, K. A. Possible High T_c Superconductivity in the Ba-La-Cu-O System. *Z. Phys. B: Cond Mat.* **1986**, *64*, 189-193.

[4] *Superconductivity*; Poole Jr, C. P., Farach, H. A., Creswick, R. J., Prozorov, R., Eds.; Academic Press, Elsevier, 2007

[5] Lee, K. H. ; Kim, S. W. ; Ohta, H. ; Koumoto, K. Ruddlesden-Popper phases as thermoelectric oxides: Nb-doped $SrO(SrTiO_3)_n$ (n = 1, 2). *J. Appl. Phys.* **2006**, *100*, 063717.

[6] Lee, K. H. ; Ishizaki, A. ; Kim, S. W. ; Ohta, H. ; Koumoto, K. Preparation and thermoelectric properties of heavily Nb-doped $SrO(SrTiO_3)_1$ epitaxial films. *J. Appl. Phys.* **2007**, *102*, 033702.

[7] Wang, Y. ; Lee, K. H. ; Ohta, H. ; Koumoto, K. Thermoelectric properties of electron doped $SrO(SrTiO_3)_n$ (n = 1, 2) ceramics. *J. Appl. Phys.* **2009**, *105*, 103701.

[8] Paranthaman, M. ; Aruchamy, A. ; Aravamudan, G. ; Subba Rao, G. V. Photoelectrochemical studies on the mixed oxides, $SrTiO_3$, Sr_2TiO_4 and $Sr_3Ti_2O_7$. *Mater. Chem. Phys.* **1984**, *14*, 349-365.

[9] Yi, Z. G. ; Iwai, H. ; Ye, J. H. Photochromism and visible light induced H_2 generation in Sr_2TiO_4: Cr complexes. *Appl. Phys. Lett.* **2010**, *96*, 114103.

[10] Castelli, I. E. ; Garcia-Lastra, J. M. ; Hüser, F. ; Thygesen, K. S. ; Jacobsen, K. W. Stability and bandgaps of layered perovskites for one- and two-photon water splitting. *New J. Phys.* **2013**, *15*, 105026.

[11] Jia, Y. ; Shen, S. ; Wang, D. ; Wang, X. ; Shi, J. ; Zhang, F. ; Han, H. ; Li, C. Composite $Sr_2TiO_4/SrTiO_3$(La,Cr) heterojunction based catalyst for hydrogen production under visible light radiation. *J. Mater. Chem. A* **2013**, *1*, 7905-7912.

[12] Sun, X. ; Xie, Y. ; Wu, F. ; Chen, H. ; Lv, M. ; Ni, S. ; Liu, G. ; Xu, X. Photocatalytic Hydrogen Production over Chromium Doped Layered Perovskite Sr_2TiO_4. *Inorg. Chem.* **2015**, *54*, 7445-7453.

[13] Shimura, T. ; Suzuki, K. ; Iwahara, H. High temperature protonic conduction in Sr_2TiO_4-based ceramics with K_2NiF_4-type structure. *Solid State Ion.* **1997**, *104*, 79-88.

[14] Sirikanda, N. ; Matsumoto, H. ; Ishihara, T. effect of Co doping on oxygen permeation in $Sr_3Ti_2O_7$ with Ruddlesden-Popper structure. *Solid State Ion.* **2011**, *192*, 599-601.

[15] Zhao, K. ; Wang, Y.-P. ; Chen, M. ; Xu, Q. ; Kim, B.-H. ; Huang, D.-P. Electrochemical evauation of $La_2NiO_{4+\delta}$ as a cathode material for intermediate temperature solid oxide fuel cells. *Internat. J. Hydrog. Energy* **2014**, *39*, 7120-7130.

[16] Ananyev, M. V. ; Tropin, E. S. ; Eremin, V. A. ; Farlenkov, A. S. ; Smirnov, A. S. ; Kolchugin, A. A. ; Porotnikova, N. M. ; Khomdichuk, A. V. ; Berenov, A. V. ; Kurumchin, E. K. Oxygen isotope exchange in $La_2NiO_{4\pm\delta}$. *Phys. Chem. Chem. Phys.* **2016**, *18*, 9102-9111.

[17] Cockroft, N. J. ; Lee, S. H. ; Wright, J. C. Site-selective spectroscopy of defect chemistry in $SrTiO_3$, Sr_2TiO_4 and $Sr_3Ti_2O_7$. *Phys. Rev. B* **1991**, *44*, 4117-4126.

[18] Inaguma, Y. ; Nagasawa, D. ; Katsumata, T. Photoluminescence of Praesodymium-Doped $Sr_{n+1}Ti_nO_{3n+1}$. *Jpn. J. Appl. Phys.* **2005**, *44*, 761-764.

[19] Mu, Z. ; Hu, Y. ; Ju, G. Luminescence properties of Eu^{2+} and Ho^{3+} in Sr_2TiO_4. *J. Rare Earth* **2012**, *30*, 744-747.

[20] Matsuno, J. ; Okimoto, Y. ; Kawasaki, M. ; Tokura, Y. Variation of the Electronic Structure in Systematically Synthesized Sr_2MO_4 (M = Ti, V, Cr, Mn, and Co). *Phys. Rev. Lett.* **2005**, *95*, 176404.

[21] Weng, H.; Kawazoe, Y. ; Wan, X. ; Dong, J. Electronic structure and optical properties of layered perovskite Sr_2MO_4 (M = Ti, V, Cr and Mn): An Ab initio study. *Phys. Rev. B* **2006**, *74*, 205112.

[22] Nakamura, M. ; Kawasaki, M. ; Tokura, Y. e_g-level splitting in a layered perovskite manganite as revealed by charge modulation spectroscopy. *Phys. Rev. B* **2012**, *86*, 125127.

[23] Sakurai, H. Synthesis Conditions and Magnetic Properties of Sr_2CrO_4 with the K_2NiF_4-type structure. *J. Phys. Soc. Jpn.* **2014**, *83*, 123701.

[24] Kim, B. J. ; Ohsumi, H. ; Komesu, T. ; Sakai, S. ; Morita, T. ; Takagi, H. ; Arima, T. Phase-Sensitive Observation of a Spin-Orbital Mott State in Sr_2IrO_4. *Science* **2009**, *323*, 1329.

[25] Haskel, D. ; Fabbris, G. ; Zhernonkov, M. ; Kong, P. P. ; Jin, C. Q. ; Cao, G. ; van Veenendaal, M. Pressure Tuning of the Spin-Orbit Coupled Ground State in Sr_2IrO_4. *Phys. Rev. Lett.* **2012**, *109*, 027204.

[26] Matsuno, J. ; Okimoto, Y. ; Fang, Z. ; Yu, X. Z. ; Matsui, Y. ; Nagaosa, N. ; Kawasaki, M. ; Tokura, Y. Metallic Ferromagnet with Square-Lattice CoO_2 Sheets. *Phys. Rev. Lett.* **2004**, *93*, 167202.

[27] Wang, X. L. ; Sakurai, H. ; Takayama-Muromachi, E. Synthesis, structures, and magnetic properties of novel Ruddlesden-Popper homologous series $Sr_{n+1}Co_nO_{3n+1}$ (n = 1, 2, 3, 4, and ∞). *J. Appl. Phys.* **2005**, *97*, 10M519.

[28] Luke, G. M. ; Fudumato, Y. ; Kojima, K. M. ; Larkin, M. I. ; Merrin, J. ; Nachumi, B. ; Uemura, Y. J. ; Maeno, Y. ; Mao, Z. Q. ; Mori, Y. ; Nakamura, H. ; Sigrist, M. Time-reversal symmetry-breaking superconductivity in Sr_2RuO_4. *Nature* **1998**, *394*, 558–561.

[29] Xia, J.; Maeno, Y. ; Beyersdorf, P. T. ; Fejer, M. ; Kapitulnik, A. High resolution polar Kerr effect measurements of Sr_2RuO_4: evidence for broken time-reversal symmetry in the superconducting state. *Phys. Rev. Lett.* **2006**, *97*, 167002.

[30] Pustogow, A. ; Luo, Y. K. ; Chronister A. ; Su, Y. S. ; Sokolov, D. A. ; Jerzembeck, F. ; Mackenzie, A. P. ; Hicks, C. W. ; Kikugawa, N. ; Raghu, S. ; Bauer, E. D. ; Brown, S. E. Constraints on the superconducting order parameter in Sr_2RuO_4 from oxygen-17 nuclear magnetic resonance., *Nature* **2019**, *574*, 72-75.

[31] Zhou, H. D. ; Conner, B. S. ; Balicas, L. ; Wiebe, C. R. Orbital-Ordering Transition in Sr_2VO_4. *Phys. Rev. Lett.* **2007**, *99*, 136403.

[32] Teyssier, J. ; Viennois, R. ; Giannini, E. ; Eremina, R. M. ; Günther, A. ; Deisenhofer, J. ; Eremin, M. V. ; van der Marel, D. Optical study of the phonons and electronic excitations in tetragonal Sr_2VO_4. *Phys. Rev. B* **2011**, *84*, 205130.

[33] Sugiyama, J. ; Nozaki, H. ; Umegaki, I. ; Higemoto, W. ; Ansaldo, E. J. ; Brewer, J. H. ; Sakurai, H. ; Kao, T.-H. ; Yang, H.-D. ; Mansson, M. Hidden magnetic order in Sr_2VO_4 clarified with μ^+SR. *Phys. Rev. B* **2014**, *89*, 020402(R).

[34] Karmakar, S. ; Mallavi, P. S. Novel P-T Phase Diagram of the Multiorbital Mott Insulator Sr_2VO_4. *Phys. Rev. Lett.* **2015**, *114*, 166402.

[35] Teyssier, J. ; Giannini, E. ; Stucky, A. ; Cerny, R. ; Eremin, M. V. ; van der Marel, D. Jahn-Teller induced nematic orbital order in tetragonal Sr_2VO_4. *Phys. Rev. B* **2016**, *93*, 125138.

[36] Burns, G. ; Dacol, F. H. ; Kliche, G. ; König, W. ; Shafer, M. W. Raman and infrared studies of Sr_2TiO_4: A material isomorphic to $(La,Sr)_2CuO_4$ superconductors. *Phys. Rev. B* **1988**, *37*, 3381-3388.

[37] Kamba, S. ; Samoukhina, P. ; Kadlec, F. ; Pokorny, J. ; Petzelt, J. ; Reaney, I. M. ; Wise, P. L. Composition dependence of the lattice vibrations in $Sr_{n+1}Ti_nO_{3n+1}$ Ruddlesden-Popper homologous series. *J. Europ. Ceram. Soc.* **2003**, *23*, 2639-2645.

[38] Goian, V. ; Kamba, S. ; Orloff, N. ; Birol, T. ; Lee, C. H. ; Nuzhnyy, D. ; Booth, J. C. ; Bernhagen, M. ; Uecker, R. ; Schlom, D. G. Influence of the central mode and soft phonon on the microwave dielectric loss near the strain-induced ferroelectric phase transitions in $Sr_{n+1}Ti_nO_{3n+1}$. *Phys. Rev. B* **2014**, *90*, 174105.

[39] Ge, W. ; Zhu, C. ; An, H. ; Li, Z. ; Tang, G. ; Hou, D. Sol-gel synthesis and dielectric properties of Ruddlesden-Popper phase $Sr_{n+1}Ti_nO_{3n+1}$ (n = 1, 2, 3, ∞). *Ceram. Int.* **2014**, *40*, 1569-1574.

[40] Burns, G. ; Dacol, F. H. ; Shafer, M. W. Raman measurement of materials with K_2NiF_4 structure. *Solid State Commun.* **1987**, *62*, 687-689.

[41] Venkastewaran, U. ; Strössner, K. ; Syassen, K. ; Burns, G. ; Shafer, M. W. Pressure dependence of the Raman modes in Sr_2TiO_4. *Solid State Commun.* **1987**, *64*, 1273-1277;

[42] Fennie, C. J. ; Rabe, K. M. Structural and dielectric properties of Sr_2TiO_4 from first principles. *Phys. Rev. B* **2003**, *68*, 184111.

[43] Huang, L.-F. ; Koocher, N. Z. ; Gu, M. ; Rondinelli, J. M. Structure Dependent Phase Stability and Thermal Expansion of Ruddlesden-Popper Strontium Titanates. *Chem. Mater.* **2018**, *30*, 7100-7110.

[44] Parker, W. D. ; Nakhmanson, S. M. Strain-induced incommensurate distortions in eptixial Ruddlesden-Popper-type Ba_2TiO_4. *Phys. Rev. B* **2013**, *88*, 035203.

[45] Music, D. ; Schneider, J. M. Elastic properties of $Sr_{n+1}Ti_nO_{3n+1}$ phases (n=1-3,∞). *J. Phys.: Cond. Mat.* **2008**, *20*, 055224.

[46] Lu, Y. ; Jia, D. ; Gao, F. ; Chen, Z. ; Hu, T. First-principles study on the elastic properties of Sr-Ti-O ceramics. *Solid State Commun.* **2014**, *182*, 43-46.

[47] Lu, Y. ; Jia, D. ; Gao, F. ; Chen, Z. ; Hu, T. First-principles calculations of the thermal properties of $SrTiO_3$ and $SrO(SrTiO_3)_n$ (n=1,2). *Solid State Commun.* **2015**, *201*, 25-30.

[48] Viennois, R. ; Giannini, E. ; Koza, M. ; Sauvajol, J.-L. Lattice dynamics of Sr_2TiO_4. *J. Phys.: Conf. Ser.* **2007**, *92*, 012172.

[49] Kawamura, K. ; Yashima, M. ; Fujii, K. ; Omoto, K. ; Hibino, K. ; Yamada, S. ; Hester, J. R. ; Avdeev, M. ; Miao, P. ; Torii, S. ; Kamiyama, T. Structural Origin of the Anisotropic and Isotropic Thermal Expansion of K_2NiF_4-Type $LaSrAlO_4$ and Sr_2TiO_4. *Inorg. Chem.* **2015**, *54*, 3896-3904.

[50] Rodriguez-Carvajal, J., Recent advances in magnetic-structure determination by neutron powder diffraction. *Phys. B* **1993**, *192*, 55-69.

[51] Sohn, J.-H. ; Inaguma, Y.; Itoh, M. ; Nakamura, T. Cooperative interaction of oxygen octahedra for dielectric properties in the perovskite-related layered compounds $Sr_{n+1}Ti_nO_{3n+1}$, $Ca_{n+1}Ti_nO_{3n+1}$ and $Sr_{n+1}(Ti_{0.5}Sn_{0.5})_nO_{3n+1}$ (n = 1, 2, 3 and ∞). *Mater. Sci. Eng. B* **1996**, *41*, 50-54.

[52] Piermiarini, G. J. ; Block, S. ; Barnett, J. D. ; Forman, R. A. Calibration of the pressure dependence of the R_1 ruby fluorescence line to 195 kbars, *J. Appl. Phys.* **1975**, *46*, 2774-2780.

[53] Koza, M. M.; Johnson, M. R.; Viennois, R.; Mutka, H.; Girard, L.; Ravot, D. Breakdown of phonon glass paradigm in La- and Ce- Fe_4Sb_{12} skutterudites. *Nat. Mater*. **2008**, *7*, 805-810.

[54] Gonze, X. ; Amadon, B. ; Anglade, P. M. ; Beuken, J. M. ; Bottin, F. ; Boulanger, P. ; Bruneval, F. ; Caliste, D. ; Caracas, R. ; Côté, M. *et al.* ABINIT: First-principles approach to material and nanosystem properties. *Comput. Phys. Comm.* **2009**, *189*, 2582-615.

[55] Teter, M. P. Additional condition for transferability in pseudopotentials. *Phys.Rev. B* **1993** *48*, 5031–5041.

[56] Gonze, X. ; Lee, C. Dynamical matrices, Born effective charges, dielectric permittivity tensors, and interatomic force constants from density-functional perturbation theory. *Phys Rev B* **1997**, *55*, 10355-68.

[57] Gonze, X. ; Charlier, J.-C. ; Allan, D. C. ; Teter M. P. Interatomic force constants from density-functional perturbation theory: the case of α-quartz. *Phys Rev B* **1994**, *50*, 13035-38.

[58] Veithen, M. ; Gonze, X. ; Ghosez, Ph. First Principles Study of Electro-optic Effect in Ferroelectric Oxides. *Phys. Rev. Lett.* **2004**, *93*, 187401.

[59] Hermet, P. ; Bantignies, J.-L. ; Rahamani, A. ; Sauvajol, J.-L ; Johnson, M. R. ; Serein, F. Far- and Mid-Infrared of Crystalline 2,2'-Bithiophene; Ab Initio Analysis and Comparison with Infrared Response. *J. Phys. Chem. A* **2005**, *109*, 1684-1691.

[60] Hermet, P. ; Gourrier, L. ; Bantignies, J.-L. ; Ravot, D. ; Michel, T. ; Deabate, S. ; Boulet, P. ; Henn, F. Dielectric, Magnetic, and Phonon Properties of Nickel Hydroxide. *Phys. Rev. B* **2011**, *84*, 235211.

[61] Hermet, P. ; Veithen, M. ; Ghosez, Ph. First-Principles Calculations of the Non-Linear Optical Susceptibilities and Raman Scattering Spectra of Lithium Niobate. *J. Phys.: Condens. Matter*. **2007**, *19*, 456202.

[62] Wu, Z. J. ; Zhao, E. J. ; Xiang, H. P. ; Hao, X. F. ; Liu, X. J. ; Mang, J. Crystal structure and elastic properties of superhard IrN_2 and IrN_3 from first principles. *Phys. Rev. B* **2007**, *76*, 054115.

[63] Pugh, S. F. Relations between the elastic moduli and the plastic properties of polycrystalline pure metals. *Philos. Mag.* **1954**, *45*, 823-843.

[64] Jund, P. ; Viennois, R. ; Tao, X. ; Niedzolka, K. ; Tedenac, J.-C. Physical properties of thermoelectric zinc antimonide using first-principles calculations. *Phys. Rev. B* **2012**, *85*, 224105.

[65] Saha, S. K. ; Dutta, G. Elastic and thermal properties of the layered thermoelectrics BiOCuSe and LaOCuSe. *Phys. Rev. B* **2016**, *94*, 125209.

[66] Jacobs, K. T. ; Rajitha, G. Thermodynamic properties of strontium titanates : Sr_2TiO_4, $Sr_3Ti_2O_7$, $Sr_4Ti_3O_{10}$ and $SrTiO_3$. *J. Chem. Thermodyn.* **2011**, *43*, 51-57.

[67] Gao, L. ; Liu, S. ; Wang, R. ; Gao, F. ; Sun, K. ; Hao, X. NaCl-CsCl structural transition in Sr_2PdO_3 and Sr_2TiO_4. *J. Alloys Compds.* **2018**, *737*, 230-237.

[68] Ulrich, C. ; Anastassakis, E. ; Syassen, K. ; Debernardi, A. ; Cardona, M. Lifetimes of Phonons in Semiconductors under Pressure. *Phys. Rev. Lett.* **1997**, *78*, 1283-1286.

[69] de Ligny, D. ; Richet, P. High temperature heat capacity and thermal expansion of $SrTiO_3$ and $SrZrO_3$ perovskites. *Phys. Rev. B* **1996**, 53, 3013.

[70] Barron, T. H. K. ; Collins, J. G. ; White, G. K. Thermal expansion of solids at low temperatures. *Adv. Phys.* **1981**, *29*, 609-730.

[71] Feng, J. ; Xiao, B. ; Zhou, R. ; Pan, W. ; Clarke, D. R. Anisotropic elastic and thermal properties of the double perovskite slab-rock layer $Ln_2SrAl_2O_7$ (Ln = La, Nd, Sm, Eu, Gd or Dy) natural superlattice structure. *Acta Mater.* **2012**, *60*, 3380-3392.

[72] Lucazeau, G. Effect of pressure and temperature on Raman spectra of solids: anharmonicity. *J. Raman Spectrosc.* **2003**, *34*, 478-496.

[73] Liarokiapis, E. ; Anastassakis, E. ; Kourouklis, G. A. Raman study of the phonon anharmonicity in LaF_3. *Phys. Rev. B* **1985**, *32*, 8346-8355.

[74] Weinstein, B. A. ; Zallen, R. *Topics in Applied Physics* **1984**, *54*, 463-527.

[75] Kourouklis, G. A. ; Anastassakis, E. Pressure induced phase transition in SrF_2. *Phys. Rev. B* **1986**, *34*, 1233-1237.

[76] Kourouklis, G. A. ; Anastassakis, E. Pressure Induced Phase Transition and Anharmonicity Study of Alkaline-Earth Fluorides. *Phys. Stat. Sol. (b)* **1989**, *152*, 89-99.

[77] Balkanski, M. ; Wallis, R. F. ; Haro, E. Anharmonic effects in light scattering due to optical phonons in silicon. *Phys. Rev. B* **1983**, *28*, 1928-1934.

Table captions

Table 1: Calculated mechanical constants C_{ij}, the bulk modulus B_h, shear modulus G_h, Young's modulus E_h (in GPa) and Poisson coefficient ν_h within the Hill approximation in Sr_2TiO_4.

Table 2: Calculated frequencies of the optical phonons (in cm^{-1}) compared to Raman and Infrared (IR) experiments. [53-55] Note that the LO modes are labelled in parentheses. In the case of Kamba's data [53], the modes labelled with * may not be true modes.

Table 3: Frequencies and Grüneisen parameters of the optical phonons (in cm^{-1}) from the Raman scattering experiments.

Table 4: Frequencies and Grüneisen parameters of the optical phonons (in cm^{-1}) from DFPT calculations.

Tables

Elastic constants	
C_{11}	308.8
C_{33}	287.4
C_{12}	73.8
C_{13}	91.1
C_{44}	72.8
C_{66}	88.3
B_h	157.5
G_h	88.6
E_h	223.8
ν_h	0.263

Table 1

Symmetry modes	A_{1g}	E_g	A_{2u}	E_u	B_{2u}
DFT (present)	216.5, 588.5	121.5, 271.5	231(253), 379(479.5), 500(685.5)	146(183.5), 217.5(226), 243(451), 609.5(789)	303
DFT [58]	216, 588	121, 271	231(252), 378(479), 499(684)	148(184), 218(227), 246(451), 611(789)	303
Raman 20 K (present)	207.8, 570	123.5, 284.5			
Raman RT (present)	204.2, 573.8	122.2, 283.8			
Raman, IR RT [56]	205, 578	124, 286	242, (467), 545(683)	151(182), 197(239), 259(467), (727)	
Raman, IR RT [53]	205.6, 574.6	123.5, 286.1	244.4(245.6), 510(529.3)*,547(686.3)	177(184), 201(210), 218(239)*, 257(470), 292(284.6)*, 701.5(743.7)	
IR 10 K, film [54]				121, 203, 305	

Table 2

Symmetry	ω_i (cm^{-1})	γ_i^T	γ_i^P	γ_i^V	η_i
E_g	122.2	2.27	1.03	-1.24	2.21
	283.8	0.77	0.29	-0.48	2.65
A_{1g}	204.2	2.26	1.62	-0.64	1.4
	573.8	1.19	0.54	-0.65	2.22

Table 3

Symmetry	ω_i (cm^{-1})	$d\omega_i/dP$ (cm^{-1}/GPa)	γ_i^T
E_g	121.5	2.14	2.78
	271.5	1.31	0.76
A_{1g}	216.5	2.73	1.98
	588.5	4.64	1.24
A_{2u} TO (LO)	231 (253)	4 (3.35)	2.73 (2.09)
	379 (479.5)	1.86 (1.03)	0.77 (0.34)
	500 (685.5)	3.99 (4.94)	1.26 (1.14)
E_u TO (LO)	146 (183.5)	3.59 (2.05)	3.87 (1.76)
	217.5 (226)	2.36 (1.71)	1.71 (1.19)
	243 (451)	2.38 (1.26)	1.55 (0.43)
	609.5 (789)	8.41 (8.79)	2.17 (1.76)
B_{2u}	303	0.45	0.23

Table 4

Figure captions

Figure 1: Rietveld refinement of the powder X-ray pattern of Sr_2TiO_4 at room temperature.

Figure 2: Experimental (20K) and calculated (0K) Raman spectra.

Figure 3: Calculated phonon dispersion curves, total and atom-projected density of states of Sr_2TiO_4. Blue corresponds to Sr, green corresponds to Ti and red corresponds to O.

Figure 4: Experimental generalized density of states of Sr_2TiO_4 from INS experiments and total phonon density of states of Sr_2TiO_4 obtained from DFPT calculations.

Figure 5: Experimental heat capacity C_P of Sr_2TiO_4 from the present work as well as Jacobs and Rajitha[89], and computed heat capacity C_V of Sr_2TiO_4 obtained from DFPT calculations.

Figure 6: Evolution of the Raman spectra with pressure (left). The asterisks correspond to the new modes appearing under high pressure. Variation of the frequencies with pressure (right). The blue solid lines are a 2nd order polynomial fit; the red dotted lines are linear fits.

Figure 7: Evolution of the Raman spectra with temperature.

Figure 8: Variation of the frequencies ω_1 (E_g), ω_2 (A_{1g}), ω_3 (E_g) and ω_4 (A_{1g}) of the Raman-active modes with temperature.

Figure 9: Variation of the FWMH Δ_1, Δ_2, Δ_3 and Δ_4 of the Raman-active modes with temperature. Experimental data are symbols, calculations with 3-phonon interactions are dotted blue lines, calculations with 3-phonon and 4-phonon interactions are solid red lines.

Figure 10: Thermal variation of the lattice parameters *a* and *c* of Sr_2TiO_4.

Figure 11: Thermal evolution of the thermal expansion coefficients α_x and α_z (top) and the volume thermal expansion coefficient α_V (bottom) of Sr_2TiO_4. Inset: thermodynamic volume Grüneisen parameter for Sr_2TiO_4, obtained using the bulk modulus computed by DFPT.

Figure 12: Variation of $\Delta\omega_1$ (E_g), $\Delta\omega_2$ (A_{1g}), $\Delta\omega_3$ (E_g) and $\Delta\omega_4$ (A_{1g}) of the Raman-active modes with temperature. Experimental data are full black squares, the quasi-harmonic implicit contribution is the solid black lines, the anharmonic explicit contribution due to 3 phonons and 4 phonons interactions is the hollow black circles. The explicit contribution fitted by calculations with 3 phonons and 4 phonons interactions are dashed red lines and the contribution of the 3 phonons interactions are dotted blue lines.

Figures

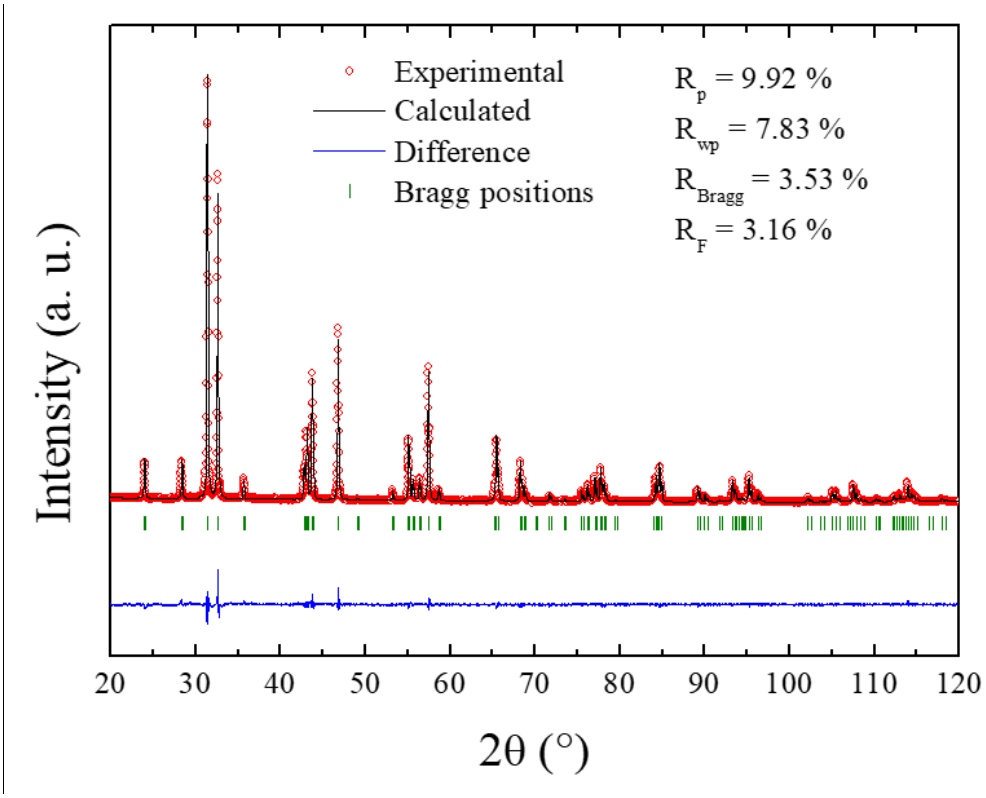

Figure 1

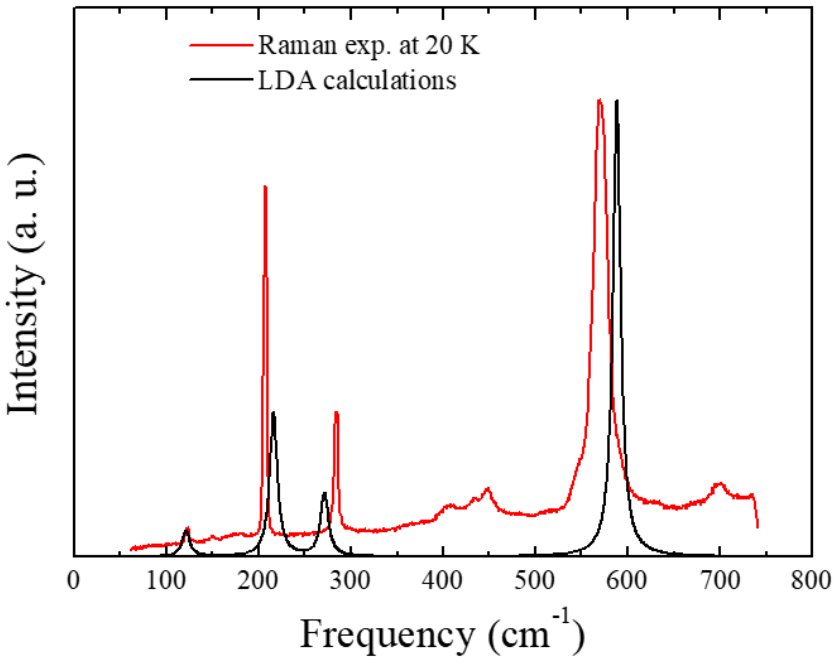
Raman exp. at 20 K
LDA calculations
Intensity (a. u.)
0
100
200
300
400
500
600
700
800
Frequency (cm-1)

Figure 2

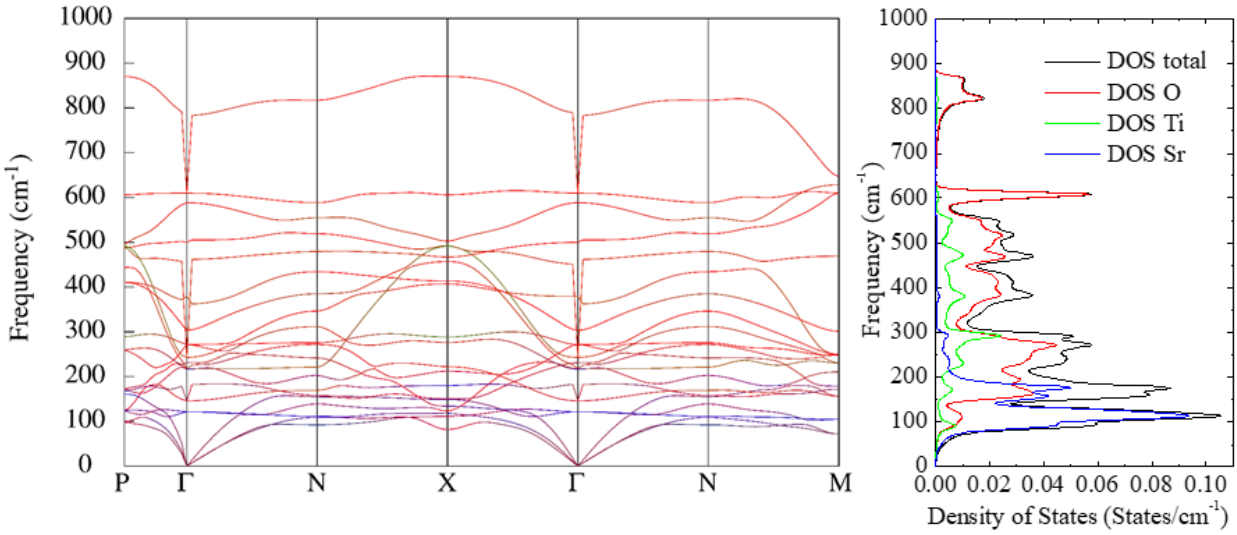
Frequency (cm-1)
1000
900
800
700
600
500
400
300
200
100
0
P
Γ
N
X
Γ
N
M
DOS total
DOS O
DOS Ti
DOS Sr
0.00 0.02 0.04 0.06 0.08 0.10
Density of States (States/cm-1)

Figure 3

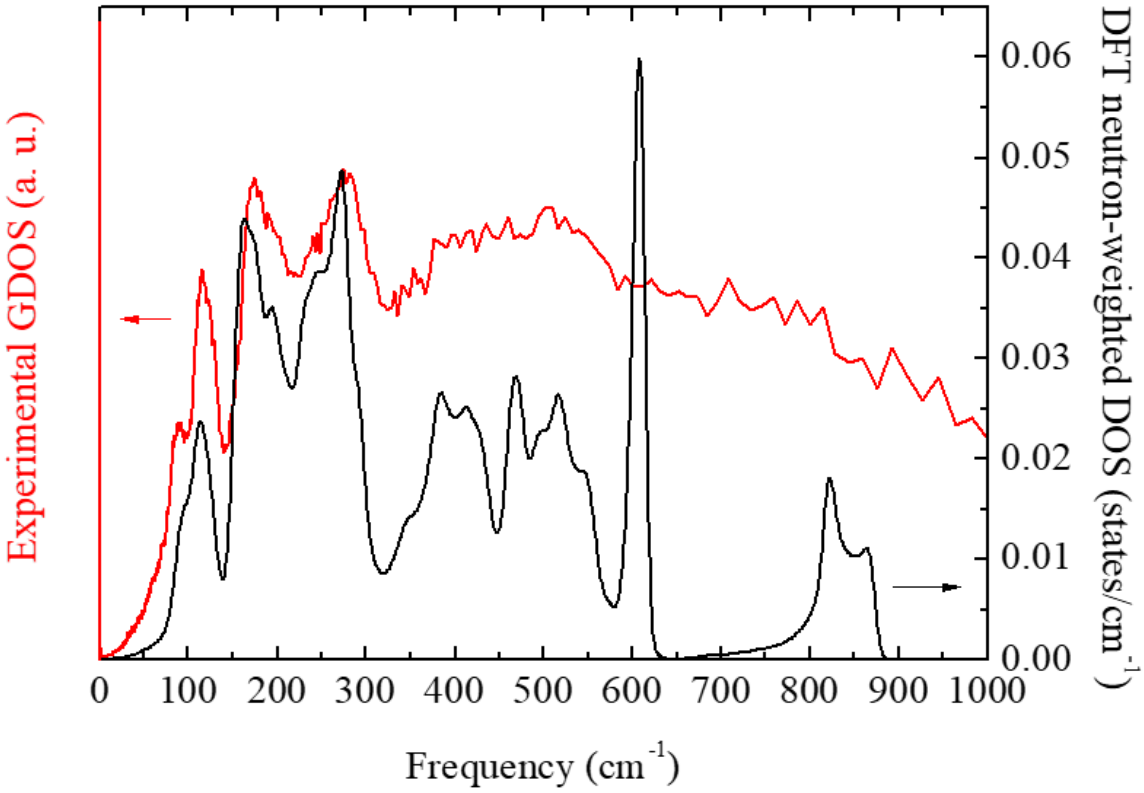
Experimental GDOS (a. u.)
DFT neutron-weighted DOS (states/cm-1)
Frequency (cm-1)
0
100
200
300
400
500
600
700
800
900
1000
0.00
0.01
0.02
0.03
0.04
0.05
0.06

Figure 4

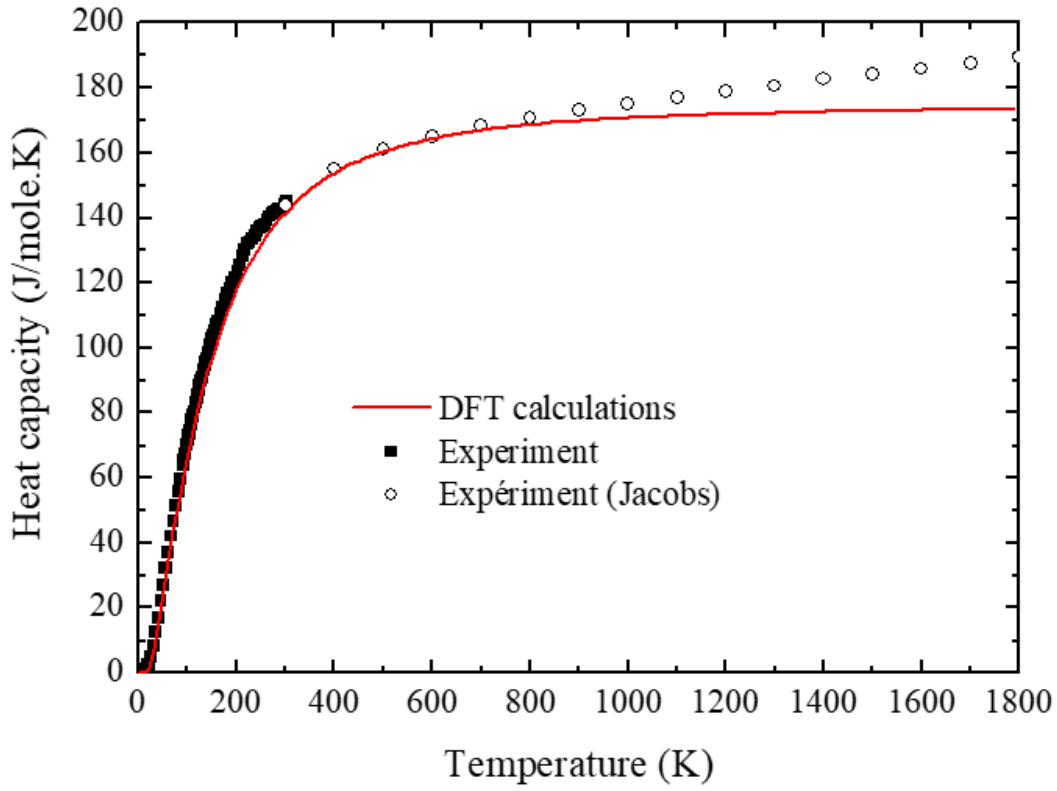
Heat capacity (J/mole.K)
Temperature (K)
DFT calculations
Experiment
Expériment (Jacobs)
0
20
40
60
80
100
120
140
160
180
200
0
200
400
600
800
1000
1200
1400
1600
1800

Figure 5

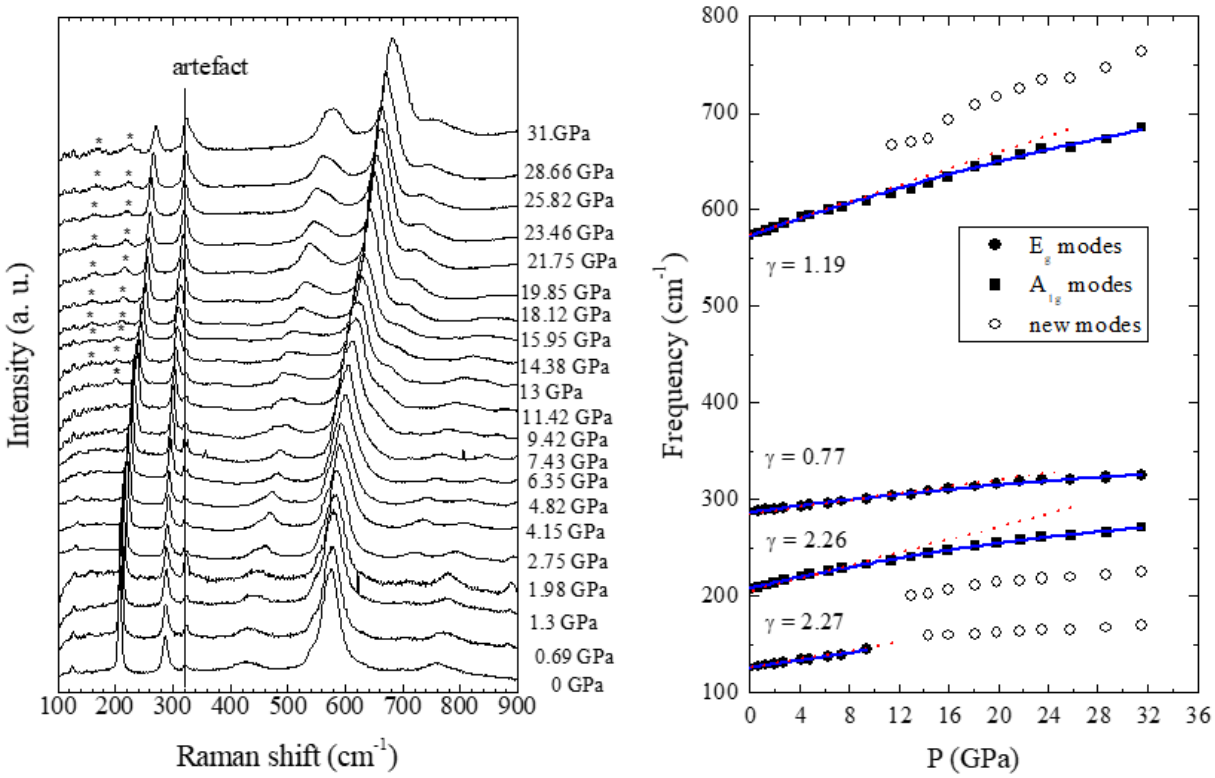
artefact
31.GPa
28.66 GPa
25.82 GPa
23.46 GPa
21.75 GPa
19.85 GPa
18.12 GPa
15.95 GPa
14.38 GPa
13 GPa
11.42 GPa
9.42 GPa
7.43 GPa
6.35 GPa
4.82 GPa
4.15 GPa
2.75 GPa
1.98 GPa
1.3 GPa
0.69 GPa
0 GPa
Intensity (a. u.)
Raman shift (cm-1)
100 200 300 400 500 600 700 800 900
Frequency (cm-1)
P (GPa)
0 4 8 12 16 20 24 28 32 36
100 200 300 400 500 600 700 800
Eg modes
A1g modes
new modes
γ = 1.19
γ = 0.77
γ = 2.26
γ = 2.27

Figure 6

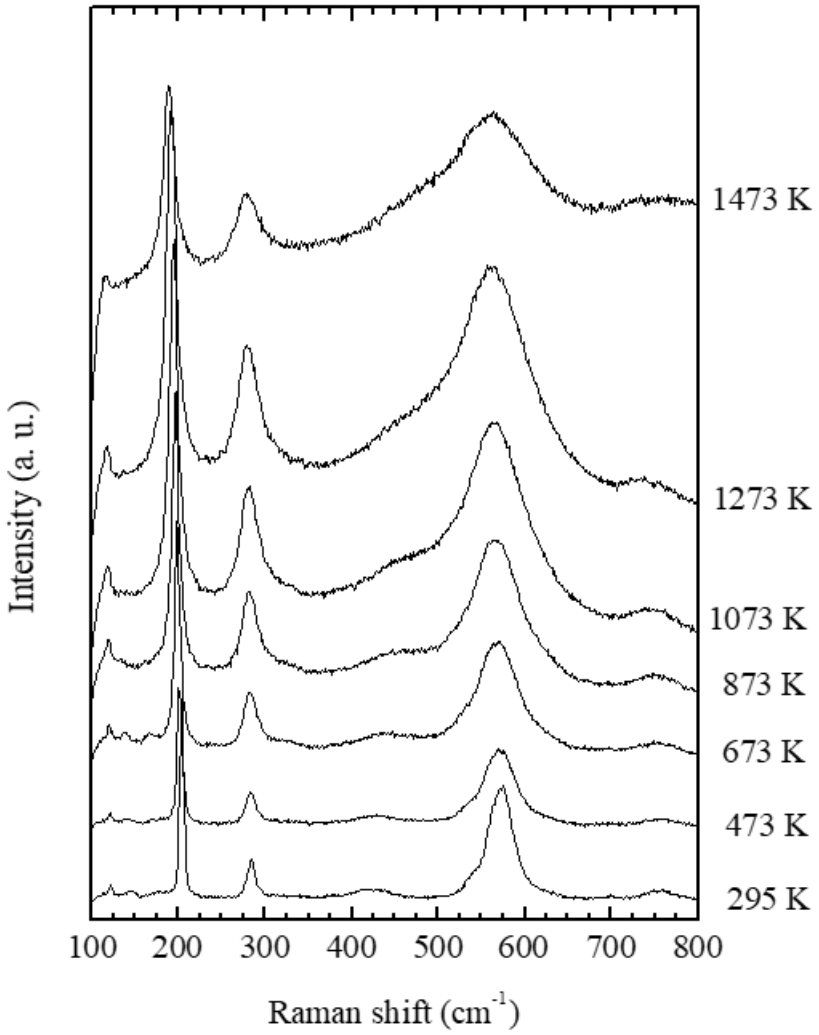
Intensity (a. u.)
1473 K
1273 K
1073 K
873 K
673 K
473 K
295 K
100
200
300
400
500
600
700
800
Raman shift (cm-1)

Figure 7

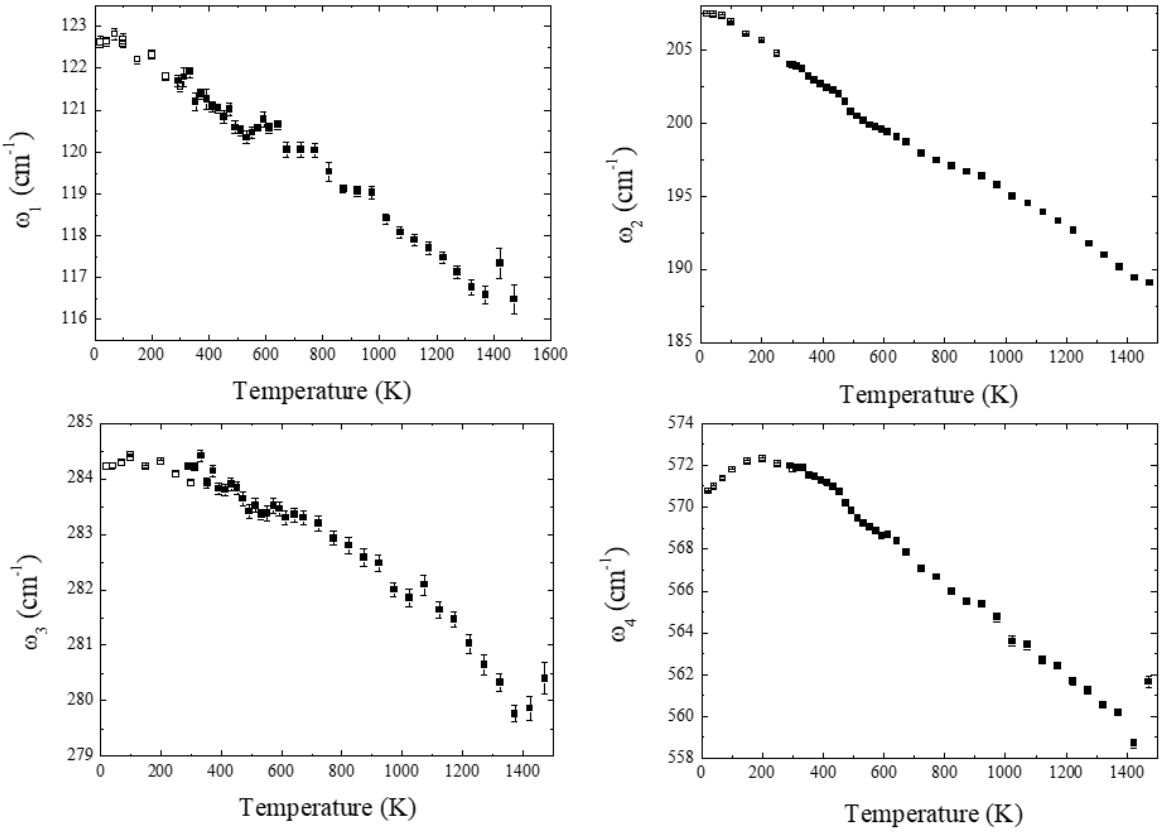
ω1 (cm-1)
Temperature (K)
ω2 (cm-1)
Temperature (K)
ω3 (cm-1)
Temperature (K)
ω4 (cm-1)
Temperature (K)

Figure 8

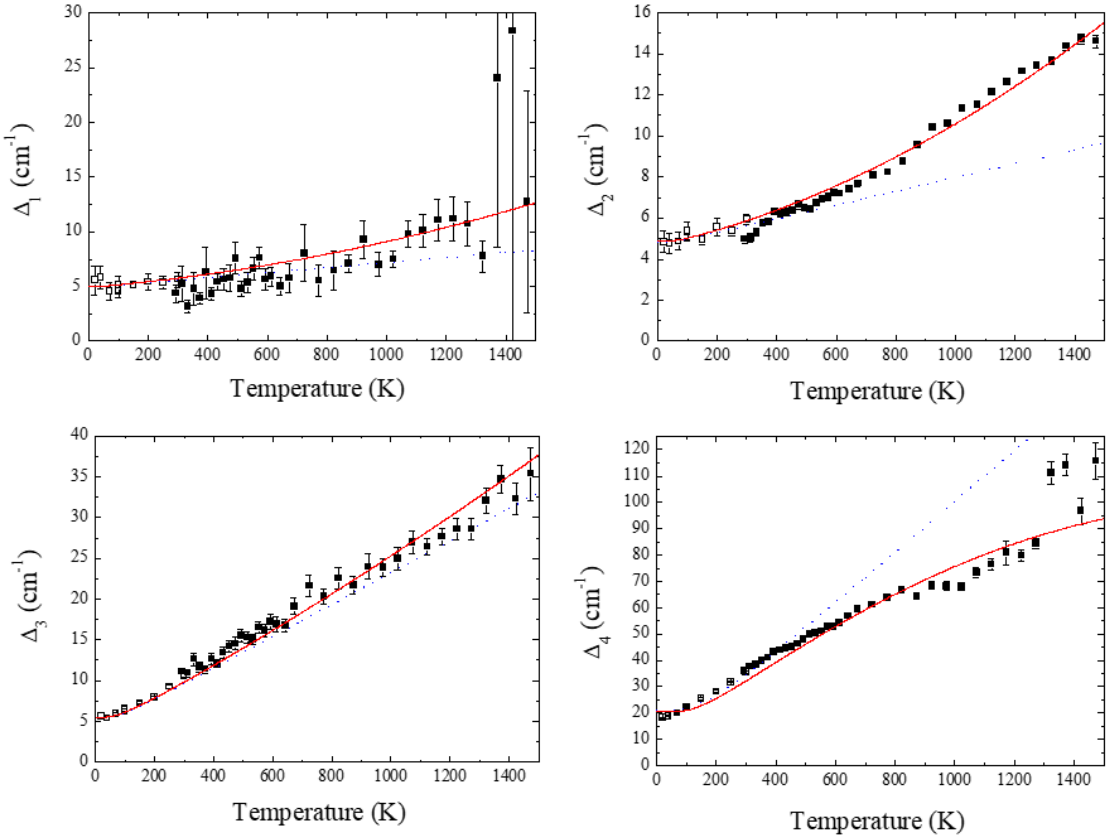

Figure 9

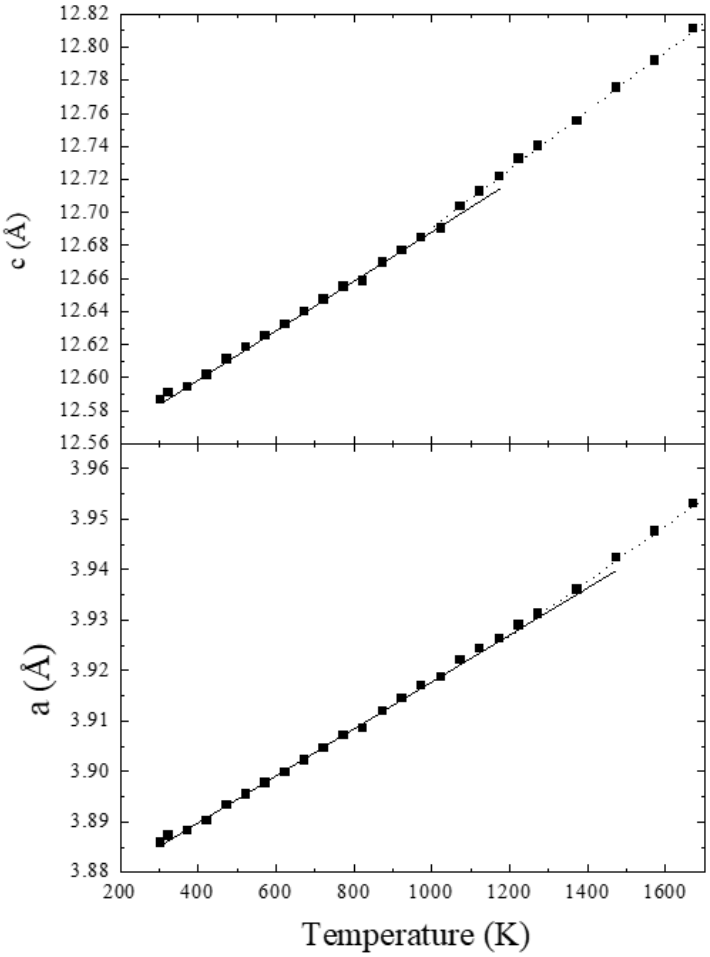
c (Å)
a (Å)
Temperature (K)
12.82
12.80
12.78
12.76
12.74
12.72
12.70
12.68
12.66
12.64
12.62
12.60
12.58
12.56
3.96
3.95
3.94
3.93
3.92
3.91
3.90
3.89
3.88
200
400
600
800
1000
1200
1400
1600

Figure 10

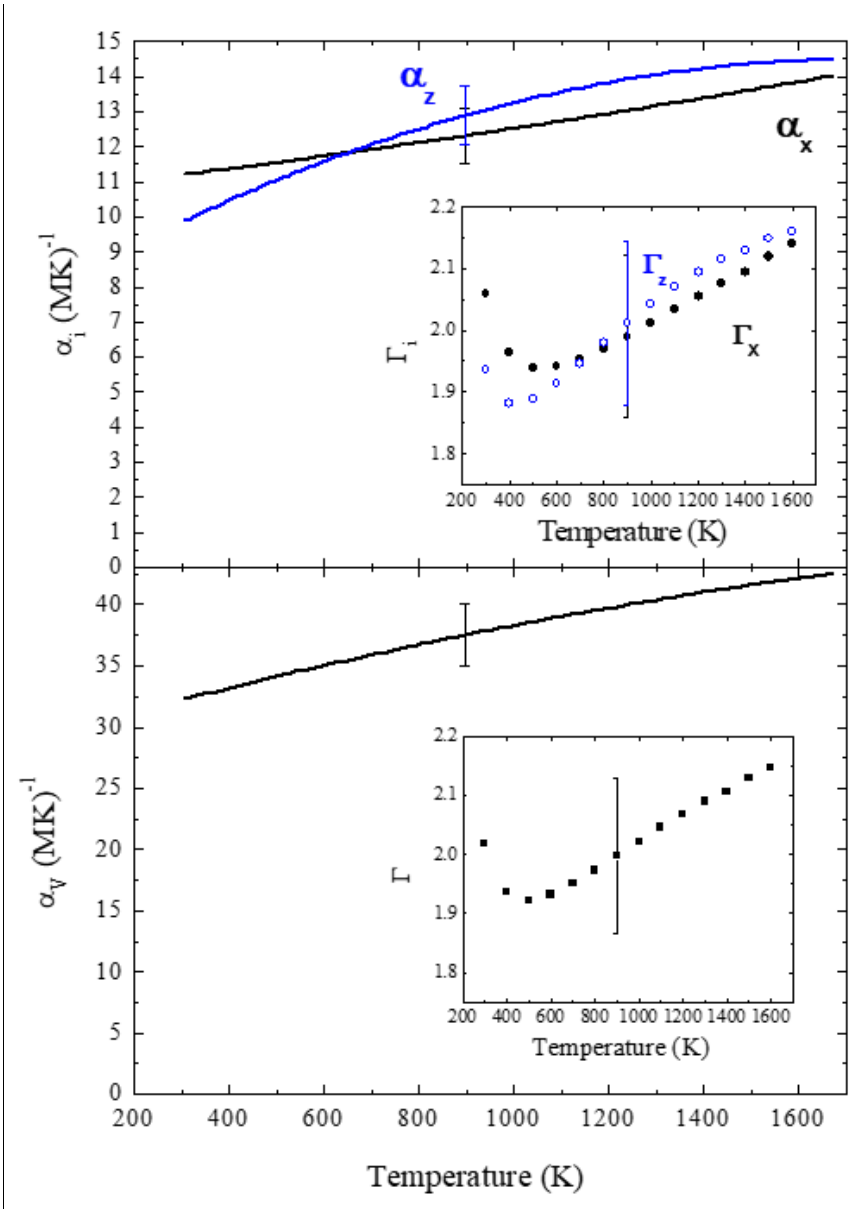

Figure 11

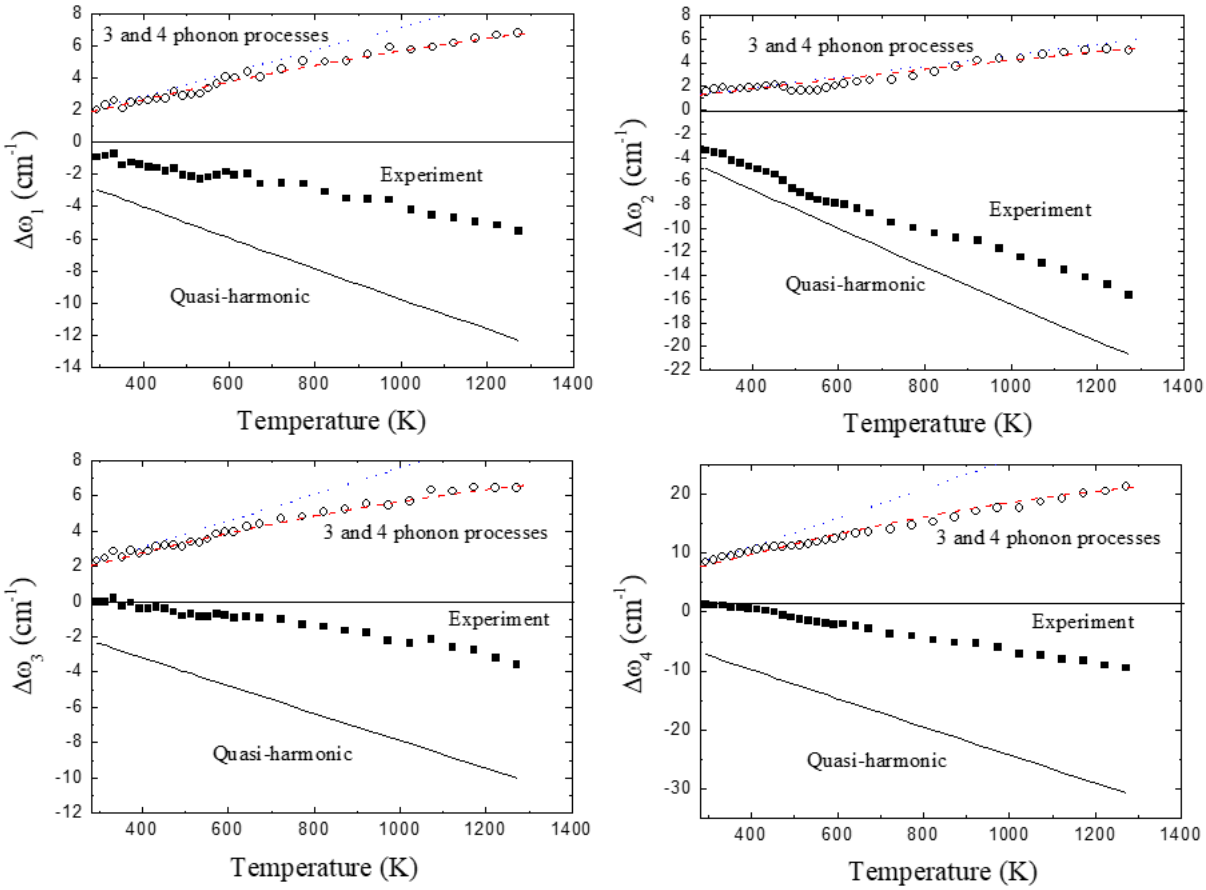
3 and 4 phonon processes
Experiment
Quasi-harmonic
Δω1 (cm-1)
Δω2 (cm-1)
Δω3 (cm-1)
Δω4 (cm-1)
Temperature (K)

Figure 12

TOC graphic

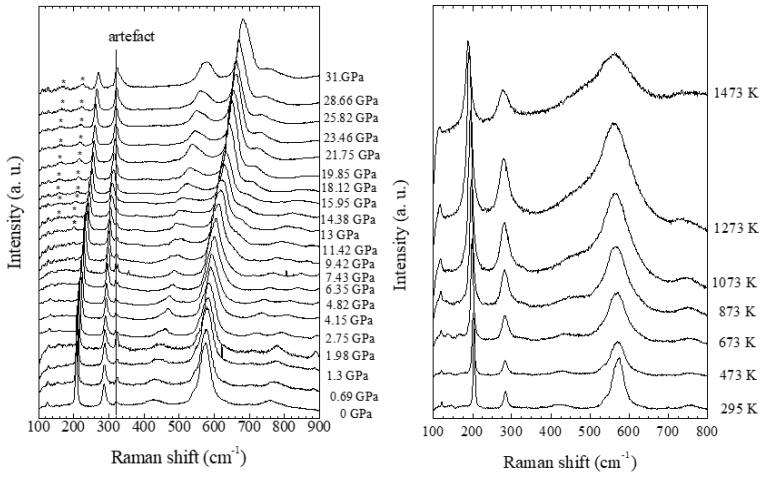
artefact
31.GPa
28.66 GPa
25.82 GPa
23.46 GPa
21.75 GPa
19.85 GPa
18.12 GPa
15.95 GPa
14.38 GPa
13 GPa
11.42 GPa
9.42 GPa
7.43 GPa
6.35 GPa
4.82 GPa
4.15 GPa
2.75 GPa
1.98 GPa
1.3 GPa
0.69 GPa
0 GPa
Intensity (a. u.)
100 200 300 400 500 600 700 800 900
Raman shift (cm-1)
1473 K
1273 K
1073 K
873 K
673 K
473 K
295 K
Intensity (a. u.)
100 200 300 400 500 600 700 800
Raman shift (cm-1)